CHAPTER 1

INTRODUCTION

The discovery of pulsars has provided us with precision tools for investigating Galactic dynamics, as probes of core collapse supernovae, as instruments to explore ultra-dense matter equations of state, and as tests of gravity. In this chapter, we will provide an introduction to gravitational waves (GWs), pulsars, pulsar timing, and GW experiments with pulsar timing arrays (PTAs).

1.1 The Gravitational Wave Universe

Colloquially known as "ripples" in spacetime, GWs are propagating metric perturbations that cause subtle changes in the distances between objects. Observations of GWs offer a new window to viewing the Universe beyond traditional electromagnetic-based astronomy. Just as we build many different kinds of telescopes to observe different frequencies of light across the electromagnetic spectrum, different classes of GW observatories spanning the separate GW spectrum frequency bands will enable us to probe particular sources and underlying physics.

The primary sources of GWs are compact objects, such as black holes, typically in binaries. PTAs observe in the low-frequency GW band and can be used to observe supermassive black hole binaries at the very centers of distant merging galaxies (Detweiler 1979; Hellings & Downs 1983; Romani 1989; Foster & Backer 1990), observations that allow us to understand dynamical processes during mergers that are not possible with electromagnetic telescopes. Other possible sources observable by PTAs include cosmic strings (Starobinskiĭ 1979; Sanidas et al. 2013) and primordial GWs from the inflationary epoch (Grishchuk 2005).

1.2   A Primer on Gravitational Waves

Just over a century ago, Einstein (1915b) developed his landmark theory of general relativity (GR), which describes the effect that mass and energy have on both space and time. Gravity is explained by the geometric curvature of spacetime, with objects following curved paths rather than experiencing an instantaneous central force as described by Newtonian theory. GR has yielded explanations for observed phenomena in disagreement with the Newtonian framework. Early in its development, it explained the anomalous advance of Mercury's perihelion precession of Mercury beyond the predictions from Newtonian mechanics (Le Verrier 1859; Einstein 1916). Apparent shifts in the position of a star due to the bending of light around the Sun observed by Eddington during the 1919 solar eclipse quickly verified Einstein's predictions and cemented the place of the theory in history (Dyson et al. 1920; Einstein 1915a).

The mathematics of GR are represented with the Einstein field equations, a set of 16 (10 unique) differential equations succinctly represented as

$$G_{\mu\nu} \equiv R_{\mu\nu} - \frac{1}{2}Rg_{\mu\nu} = \frac{8\pi G}{c^4}T_{\mu\nu}, \qquad (1.1)$$

where the left hand side describes the geometric curvature of spacetime and the right hand side describes the local source energy and momentum distribution multiplied by fundamental constants. Here, $G_{\mu\nu}$ is the Einstein tensor, containing terms that include the metric tensor $g_{\mu\nu}$ which determines the spacetime interval between two points, and functions of derivatives of the metric in both the Ricci tensor $R_{\mu\nu}$ and the Ricci scalar curvature R. The stress-energy tensor $T_{\mu\nu}$ contains terms for the density and flux of both energy and momentum. In normal spacetime, all tensors in Eq. 1.1 are symmetric 4×4 tensors, e.g., the indices $\mu, \nu \in \{0, 1, 2, 3\}$ are four arbitrary coordinates, one in time and three in space.

In the linearized gravity regime, we can write the Einstein field equations as

$$\Box \bar{h}_{\mu\nu} = -\frac{16\pi G}{c^4} T_{\mu\nu}, \tag{1.2}$$

where $\Box \bar{h}_{\mu\nu}$ represents the GW propagation with the usual wave operator. For more details, see the appendix to this chapter. We can use Eq. 1.2 to derive useful scaling relations for two orbiting point masses emitting GWs. Given two masses M orbiting at a separation R with a characteristic timescale (period) T and observed at a distance D, it can be shown (by dimensional analysis or again see the appendix for this derivation) that the GW strain is approximately

$$h \sim \frac{G}{Dc^4} \frac{MR^2}{T^2} \sim \frac{G}{Dc^4} MR^2 f^2 \sim \frac{G}{4\pi^2 Dc^4} MR^2 \Omega^2, \tag{1.3}$$

where f is the frequency of emission (Ω is the angular orbital frequency). In the Newtonian limit, we use the Keplerian orbital frequency to relate $\Omega^2 \sim GM/R^3$ and thus we arrive at

$$
\begin{aligned}
h \quad &\sim \quad \frac{(GM)^2}{4\pi^2 c^4 DR} \\
&\approx \quad 6 \times 10^{-16} \left(\frac{M}{10^8 M_\odot}\right)^2 \left(\frac{\text{Mpc}}{D}\right) \left(\frac{\text{mpc}}{R}\right),
\end{aligned}
\tag{1.4}
$$

where the mpc separation is roughly when the energy loss of the system is dominated by GW emission. The GW frequency is given by

$$
\begin{aligned}
f \quad &\sim \quad \frac{1}{2\pi} \left(\frac{GM}{R^3}\right)^{1/2} \\
&\approx \quad 100 \text{ nHz} \left(\frac{M}{10^8 M_\odot}\right)^{1/2} \left(\frac{\text{mpc}}{R}\right)^{3/2}.
\end{aligned}
\tag{1.5}
$$

Fiducial values are for expected supermassive black hole binaries in merging galaxies in local galaxy clusters that are in the final stages of the GW-dominated inspiral.

We can relate the GW strain to the timing precision required from a pulsar. Relating the GW to the fractional change in distance ($h \sim \Delta L/L$), for a given h,

we need to keep track of the position of a pulsar to well within ΔL. We thus have

$$
\begin{aligned}
\Delta L \quad &\sim \quad hL \sim hcT \\
&\approx \quad 9.5 \text{ m} \left(\frac{h}{10^{-16}} \right) \left(\frac{T}{10 \text{ yr}} \right),
\end{aligned}
\tag{1.6}
$$

where $L \sim cT$ is the length from the light/GW travel time. The timing precision is then trivially found to be

$$
\begin{aligned}
\Delta t \quad &\sim \quad \frac{\Delta L}{c} \sim hT \\
&\approx \quad 32 \text{ ns} \left(\frac{h}{10^{-16}} \right) \left(\frac{T}{10 \text{ yr}} \right).
\end{aligned}
\tag{1.7}
$$

Therefore, we require timing precision at the nanosecond level from pulsars in order to measure the effects of passing GWs.

1.3   The Discovery of Pulsars

Baade & Zwicky (1934) first described the theoretical possibility of a neutron star, a small, dense object composed primarily of neutrons originating as a stellar remnant from a supernova; such an object could support itself from gravitational collapse beyond the Chandrasekhar (1931) limit. The idea of neutron stars remained a theoretical curiosity through the middle of the 20th century, it took many decades before their existence could be observationally confirmed. The field of pulsar astronomy came into existence in 1967, when graduate student Jocelyn Bell (Burnell) detected a celestial pulsed signal at a radio frequency of 81.5 MHz at the Mullard Radio Astronomy Observatory near Cambridge, UK (Hewish et al. 1968). Temporarily named LGM-1 for "little green men" in reference to a possible though unlikely transmission from an extraterrestrial intelligence, the radio source was quickly theorized to be associated with a rapidly rotating neutron star (Gold 1968; Pacini 1968; Gold 1969). Confirmation came with the discovery of regular

pulsations from the Crab Nebula supernova remnant and the measurement of a steady slow down in its spin rate (Staelin & Reifenstein 1968; Comella et al. 1969; Richards & Comella 1969).

While all neutron stars are extraordinary objects, it was the discovery of the subclass of recycled, millisecond pulsars (MSPs) that truly allowed for precision timing experiments. Backer et al. (1982) discovered B1937+21, with a period of 1.558 ms, at Arecibo Observatory, an order of magnitude smaller than the period of the young Crab pulsar. It remains one of the fastest spinning pulsars known, as well as one of the most precisely timed. Since then, several hundred MSPs have been discovered, and their extreme spin stability has opened the door to a wide range of tests of fundamental physics previously discussed.

1.4 Basic Properties of Pulsars

The most fundamental observables of pulsars are the spin period P and period derivative $\dot{P}$. Different populations of pulsars fill different areas of this phase space. Figure 1.1 shows the phase space in the form of the $P - \dot{P}$ diagram with data taken from Manchester et al. (2005)[1] and Olausen & Kaspi (2014)[2]. The region in the center contains canonical pulsars (CPs), those with moderate (~ 1 s) periods and radio emission powered by rotation. CPs start their lives in the top left of the figure, at low P and high $\dot{P}$, and travel toward the bottom right (longer but more slowly changing periods); the solid lines denote characteristic ages of the pulsar assuming rotational energy is converted entirely into magnetic dipole radiation and the magnetic field strength is constant. When CPs move to the lower right, the emission mechanism shuts off and they cross the pulsar "death

---

[1] http://www.atnf.csiro.au/research/pulsar/psrcat
[2] http://www.physics.mcgill.ca/~pulsar/magnetar/main.html

line" into the shaded "graveyard" region. Note that the region is ill-defined and is a function of the emission mechanism itself. Once they cross into the region, the "dead" objects cease being observable radio pulsars. For neutron stars with a main-sequence binary companion, when the companion begins to evolve off the main sequence and increase in size, mass transfer can occur onto the neutron star. The process of accretion will spin up neutron stars to millisecond periods and reactivate the emission mechanism. Once fully "recycled" in this manner, MSPs can become extremely spin stable, have a small period derivative, and act as extremely accurate and precise clocks. Magnetars, whose primary energy reservoir is in their magnetic fields, are shown in the top right.

Dispersion in the ionized interstellar medium results from a frequency-dependent refractive index, resulting in pulses being delayed as a function of radio frequency ν, with lower frequency emission traveling slower than higher frequency emission. The dispersive delay from infinite frequency is $\Delta t \propto \mathrm{DM}/\nu^2$, where DM is the dispersion measure, equal to $\int_0^L n_e dl$, the integral of the electron density along the line of sight. Figure 1.2 shows the dispersive delay as a function of frequency for PSR J1713+0747 and the effect of proper de-dispersion. DM is another fundamental observable of pulsars observed at multiple radio frequencies, although precision estimation of DM is non-trivial (see Chapter 3 and Cordes et al. 2016).

Precise time-tagging of pulses from pulsars is performed by standard signal processing methods tied to accurate timekeeping. Individual pulse shapes appear very different but average together into a stable pulse profile. Such a waveform is used as a template in matched filtering of new pulse profile data, a procedure that finds the optimal pulse time of arrival (TOA) assuming that the observed pulse at an epoch is a noisy version of the template. In general, bright pulsars with sharp features in their template shapes and short periods will perform better as
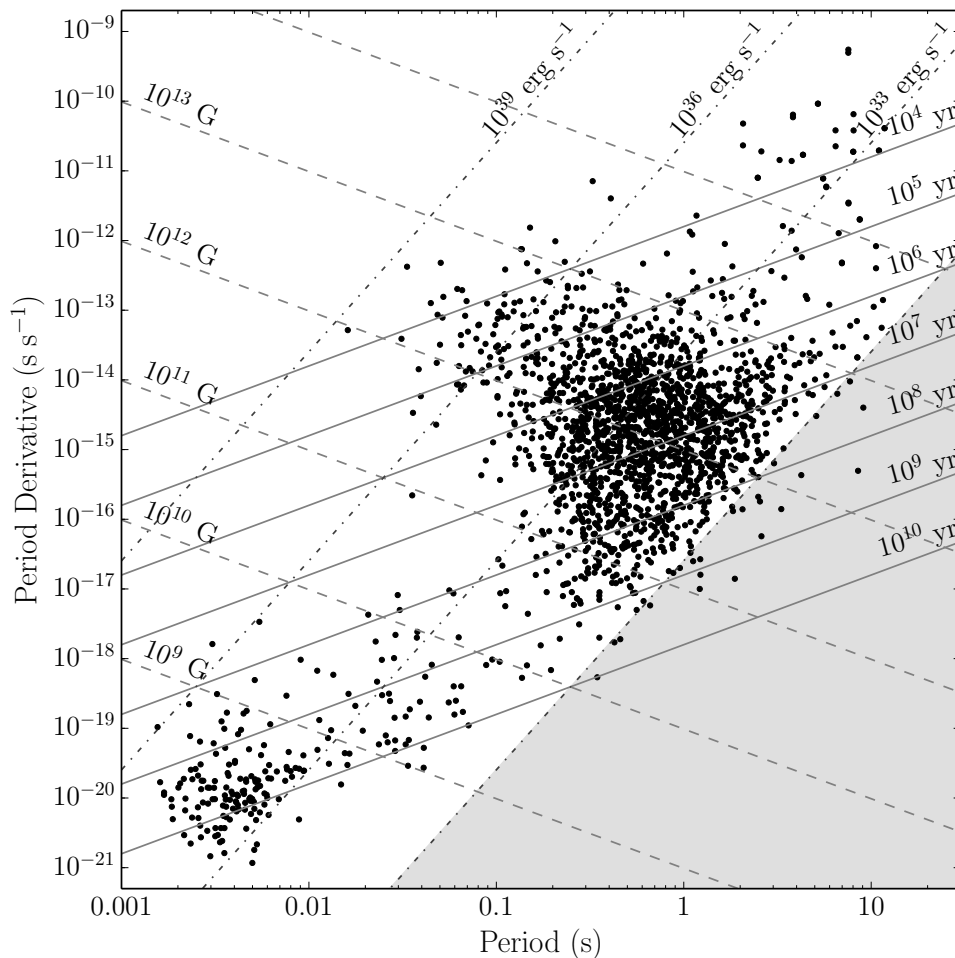
Figure 1.1: $P - \dot{P}$ diagram. The central region shows canonical pulsars while the top right shows magnetars and the bottom left shows millisecond pulsars. Lines of constant characteristic age (solid), surface magnetic field (dashed), and spin-down luminosity (the loss rate of rotational energy given the assumption of complete conversion of rotational energy into radiation; dashed-dotted) are overplotted. The shaded gray region is the pulsar graveyard, with the boundary at the "death line". Data are taken from Manchester et al. (2005) and Olausen & Kaspi (2014).

precision clocks. Since signal-to-noise ratios (S/Ns) for single pulses from typical MSPs are relatively low, many pulses are averaged together in a process known as folding. The procedure assumes a well-known initial timing model for the pulsar such that smearing of the pulse across frequency is minimized. See Chapter 5 for more details on the topics discussed here.
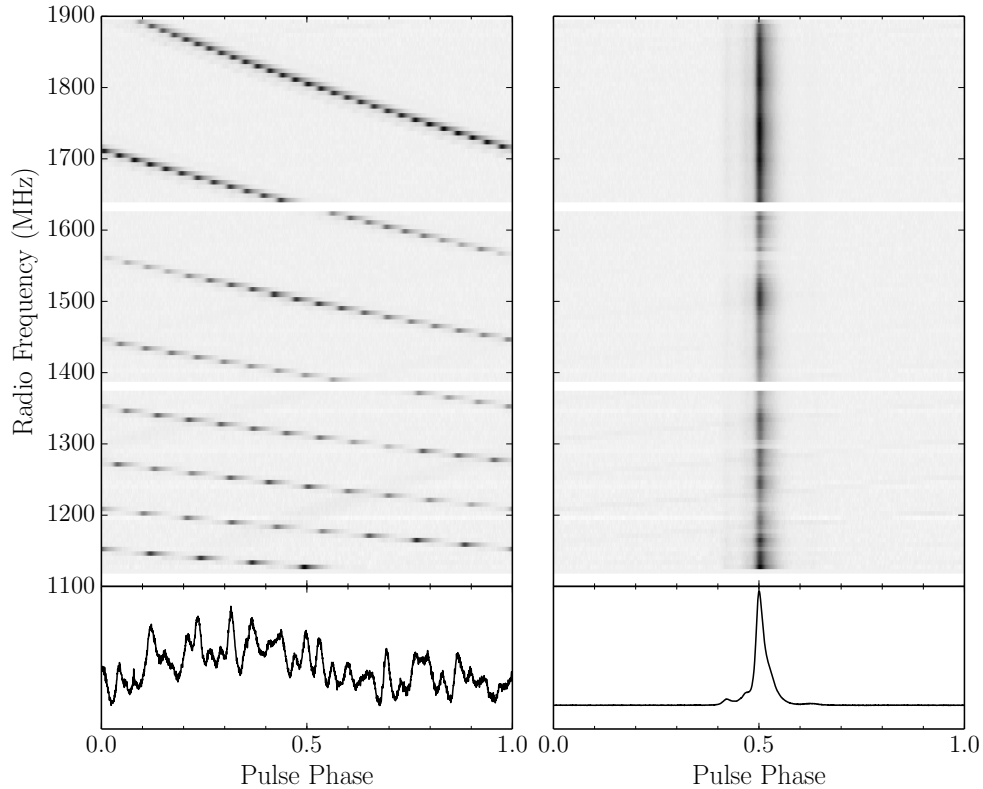
Figure 1.2: Example of dispersion in pulses with data taken from the Green Bank Telescope for the 24-hour global campaign on PSR J1713+0747. The panels on the left show dispersed pulses (with wraps in phase due to pulse folding) while the panels on the right show de-dispersed and aligned pulses. The pulses have been coherently de-dispersed within each of the 6.25 MHz frequency channels. The two horizontal gaps are pre-masked radio frequency interference from a Global Positioning System satellite (signal at ~ 1620 MHz and its reflection lower in the band). Top: Radio pulses as a function of frequency and pulse phase. Bottom: Pulses summed over all frequencies.

Precision pulsar timing relies on our ability to accurately track each rotation of the pulsar over a baseline of many years. Using both the TOAs and an initial timing model, we can update and introduce new parameter estimates that describe the kinematics of the pulsar-observatory system. In addition to the timing model parameters, we obtain timing residuals from the fit, defined as the difference be-

tween the data (pulse TOAs) and the timing model. Residuals allow models to be updated over time. They also contain useful information about the noise processes and allow us to properly characterize the noise model separately from the timing model. Residuals often show noise inconsistent with errors from the template fitting of a finite S/N pulse alone.

1.5   Tests of Gravity with Pulsars

1.5.1   Measurements of Post-Newtonian Gravity

High-precision pulsar timing experiments have allowed for a number of extremely stringent constraints on GR. One common method of placing constraints is in the Parameterized Post-Newtonian (PPN) formalism, where various order post-Newtonian corrections to classical gravity quantify physically-motivated deviations from GR. See Will (2014) for an overview of the 10 PPN parameters. Pulsar timing has provided some of the strongest constraints on a number of the PPN parameters.

The three α parameters measure if there exist preferred-frame effects. The current best limit on $\alpha_1 = 4 \times 10^{-5}$, which causes a polarization of the pulsar's eccentricity vector, comes from PSR J1738+0333 (Shao & Wex 2012). Non-zero α_2 causes spin precession and alters the pulsar's observed orbital inclination. The non-detection of precession in the pulse profile shapes of two pulsars led to a limit of $\alpha_2 < 1.6 \times 10^{-9}$ at the 95% confidence level (Shao et al. 2013). The parameter α_3, which measures violations of total momentum conservation, is the most stringent PPN constraint, with a value 4×10^{-20} from a set of measured anomalous eccentricities in MSP binary orbits (Stairs et al. 2005).

A similar analysis of stable pulse profile shapes as with α_2 allowed a limit on ξ, representing anisotropies within gravitational interactions, equal to $\xi < 3.9 \times 10^{-9}$

also at the 95% level (Shao & Wex 2013). Both α_3 and ζ_2 measure violations of total momentum conservation in the form of self-acceleration of a binary center of mass. Since α_3 is so strongly constrained, its contribution to the self-acceleration is negligible, allowing the upper limit on ζ_2 to be measured at the 4×10^{-5} level (Will 1992).

Other constraining tests of gravity have been possible with pulsar timing. As an example, Zhu et al. (2015) placed constraints on temporal changes in the gravitational constant G close to the limit from Lunar Laser Ranging (Hofmann et al. 2010) and over a significantly longer baseline. Tests of Strong Equivalence Principle violations in the strong-field limit were set by the circularity of binary systems in the Galactic potential, with the parameter $\Delta < 5.6 \times 10^{-3}$ (Stairs et al. 2005).

1.5.2 Indirect evidence of GWs

Observational evidence for the existence of GWs first came from pulsar timing experiments. Hulse & Taylor (1975) discovered the first double neutron star system, B1913+16, at Arecibo, which eventually led to the 1993 Nobel Prize in Physics. A tight binary with an orbital period of 7.75 hours, the system is losing angular momentum by radiating away energy that is not detected in the electromagnetic spectrum. The loss is inferred to be in the form of GWs, with the period becoming smaller and the size of the orbit shrinking by about 1 cm per year (Weisberg et al. 2010). The decay of the period matched the prediction from GR, with the observed-to-predicted rate of decay ratio equal to 0.96 ± 0.09, without taking into account an additional kinematic correction to the observed rate from the Galactic potential (Taylor & Weisberg 1982). Later work continued to refine the ratio, with the value of the ratio now measured to be 0.997 ± 0.002, a much more stringent constraint on GR (Taylor & Weisberg 1989; Weisberg et al. 2010).

1.5.3   Pulsar Timing Arrays

The concept of a pulsar timing array experiment for the detection of GWs dates back to the realization that Doppler tracking of several spacecraft within the solar system simultaneously could allow for a detection of GWs (Estabrook & Wahlquist 1975). It was soon realized that regular, pulsed emission could be used in the detection of low-frequency GWs as the time interval between pulses changed (Sazhin 1978; Detweiler 1979). Correlations between arrival times of pulses from an array of pulsars could be used to detect GWs of order nanohertz frequencies from merging supermassive black hole binaries (see Eqs. 1.4, 1.5; Hellings & Downs 1983; Romani 1989; Foster & Backer 1990).

Currently, three pulsar timing array experiments are underway, run by the North American Nanohertz Observatory for Gravitational Waves (NANOGrav; McLaughlin 2013), the European Pulsar Timing Array (EPTA; Kramer & Champion 2013), and the Parkes Pulsar Timing Array (PPTA; Hobbs 2013; Manchester et al. 2013). All three collaborations combine their data in a global effort called the International Pulsar Timing Array (IPTA; Hobbs et al. 2010; Manchester & IPTA 2013).

Pulsar timing will result in the direct detection of low-frequency GWs in the near future. The first direct detection of GWs in the hertz-kilohertz band has recently come from the Laser Interferometer Gravitational-Wave Observatory (LIGO; Abbott et al. 2016a). They announced the detection of GWs coming from merging stellar mass black holes (more massive than previously predicted) with a signal strong enough to be visible by eye among the noise. Besides these two types of experiments, the Laser Interferometer Space Antenna (LISA) is a future space-based LIGO analog designed primarily to observe microhertz-hertz GWs from massive black hole binaries and extreme mass ratio inspirals (massive black

holes with small compact object companions). In addition, very-low-frequency GWs ($sim 10^{-16}$ Hz range) currently are being probed by cosmic microwave background experiments. All four bands will need to be observed in order to detect sources across the full GW spectrum.

LIGO has demonstrated the need for a complete understanding of the detector and the contributing noise sources in order to properly attribute an observed signal to a GW source. During the initial LIGO run, the characterization of the noise model demonstrated their understanding of both the instrumental systematics and their low sensitivity during that phase of the project; they indeed detected no astrophysical signal at that time. Upgrades to the facility have lowered the noise floor, with current sensitivity allowing them to make the first few detections (see also Abbott et al. 2016b). Further improvements will allow LIGO to become an extremely sensitive GW instrument. Similarly, we require an understanding of the noise sources within the PTA, as the signal propagates from the pulsar through the interstellar medium to the telescope, so that we can confidently detect and then regularly observe GWs.

1.6   Characterization of Pulsar Timing Arrays

This dissertation describes efforts to understand a PTA as a Galactic-scale detector. We want to first characterize our detector and eventually improve it, for both the initial detection of GWs and long-term observations using PTAs. This work focuses on all aspects of pulse propagation through the detector. In Chapter 2, we discuss a multi-telescope campaign that observed one of the best-timed pulsars. We describe the timing errors that result from non-simultaneous multi-frequency observations and the resultant mis-estimation of the pulse dispersion measure (DM) in Chapter 3. We next investigate causes of DM variations from a

variety of effects in Chapter 4, including linear trends, periodic or quasi-periodic changes, and stochastic variations. In Chapter 5, we develop a white noise budget for pulse TOAs on short ($\lesssim 1$ hour) timescales, characterizing the timing precision of the NANOGrav MSPs. In Chapter 6, we investigate the timing noise excess beyond the white noise model and update scaling relations of the excess noise as a function of fundamental pulsar observables, moving us towards a comprehensive noise model for the NANOGrav MSPs. In Chapter 7, we present future avenues for research into the further characterization and calibration of our pulsar timing GW detector. Finally, in chapter 8, we summarize our conclusions. We also include a number of appendices at the end as reference material. Appendix A documents the PyPulse program, a set of software tools developed primarily for handling of pulse profile data purely in Python. Appendix B documents Quicklook, a program built with PyPulse for the rapid data processing and inspection of pulse profiles and their related data products.

1.7 Appendix

Here we will derive the result of Eqs. 1.2 and 1.3. First, we will consider GR for isolated systems, which can be approximated in two limits. Consider some source of gravity of mass $\sim \mathcal{M}$ and size $\sim \mathcal{R}$ that is varying on a timescale $\sim \mathcal{T}$. We define the dimensionless parameters

$$\hat{c} = \frac{c\mathcal{T}}{\mathcal{R}}, \quad \hat{G} = \frac{G\mathcal{M}\mathcal{T}^2}{\mathcal{R}^3}, \tag{1.8}$$

in a system where we choose the units such that $\mathcal{M} \sim \mathcal{R} \sim \mathcal{T} \sim 1$ and $\hat{G} \sim G$, $\hat{c} \sim c$. We can estimate the strength of gravity with the dimensionful compactness parameter (the ratio of the gravitational binding energy to the rest energy) $\epsilon \sim E_g/\mathcal{M}c^2 \sim \Phi/c^2 \sim GM/\mathcal{R}c^2 \sim \hat{G}/\hat{c}^2$, where Φ is the gravitational potential. In

the low-speed limit $\epsilon \sim (v/c)^2 \ll 1$ ($\hat{G}$ fixed), it is useful to expand Φ in powers of $1/\hat{c}$. The $\mathcal{O}(1)$ term yields the Newtonian limit for gravity while the $\mathcal{O}(1/\hat{c}^2)$ term yields what is known as post-1-Newtonian gravity, with higher order terms yielding higher post-Newtonian corrections. However, in the low source gravity limit when when $\hat{G}$ is small ($\mathcal{O}(\hat{G})$, $\hat{c}$ fixed), we obtain the linearized gravity formalism useful for describing GWs. In the $\hat{G} \rightarrow 0$ limit, we recover the equations of motion for special relativity. Both limits are useful for simply describing a wide range of different phenomena.

GWs are derived from plane-wave solutions in the linearized gravity framework. For clarity, we define our coordinates such that $x^\mu = (ct, x, y, z)$ and the Minkowski metric is $\eta_{\mu\nu} = \text{diag}(-1, 1, 1, 1)$. We can approximate the metric in the weak-field limit as flat, Minkowski spacetime with a small perturbation metric added,

$$g_{\mu\nu} = \eta_{\mu\nu} + h_{\mu\nu} + \mathcal{O}([h_{\mu\nu}]^2), \quad |h_{\mu\nu}| \ll 1. \tag{1.9}$$

We will ignore all higher-order (non-linear) terms of $h_{\mu\nu}$. It is convenient to define the trace-reversed metric perturbation as

$$\bar{h}_{\mu\nu} \equiv h_{\mu\nu} - \frac{1}{2} h \eta_{\mu\nu} \tag{1.10}$$

while choosing the Lorenz gauge such that $\partial^\mu \bar{h}_{\mu\nu} = 0$. We note that $h = \eta^{\mu\nu} h_{\mu\nu}$ and therefore $\bar{h} = -h$ and is in "trace-reversed" form. With our choice of gauge, the linearized Einstein field equations are then, after combining Eqs. 1.1 and 1.10, we arrive at Eq. 1.2, which we again write as

$$\Box \bar{h}_{\mu\nu} = -\frac{16\pi G}{c^4} T_{\mu\nu}. \tag{1.11}$$

In vacuum far away from any source, the right hand side is zero and we arrive at the usual form of the wave equation, $\Box \bar{h}_{\mu\nu} = 0$. Given the vacuum assumption, we can write the metric perturbation in the transverse-traceless (TT) gauge, such

that it is purely spatial ($h_{0\nu}^{\mathrm{TT}} = 0$), transverse to the direction of motion ($\partial^\mu h_{\mu\nu}^{\mathrm{TT}} = 0$), and traceless ($\eta^{\mu\nu} h_{\mu\nu}^{\mathrm{TT}} = h^{\mathrm{TT}} = 0$). We note that the trace-reversed metric perturbation, again assuming the vacuum solution, will equal the original metric perturbation in the transeverse-traceless gauge ($\bar{h}_{\mu\nu}^{\mathrm{TT}} = h_{\mu\nu}^{\mathrm{TT}}$) and so we will drop the "bar" for convenience.

We can write the usual *ansatz* for the wave equation solution as

$$h_{\mu\nu}^{\mathrm{TT}} = \mathrm{Re}\left[C_{\mu\nu} e^{ik_\lambda x^\lambda} \right] = \mathrm{Re}\left[C_{\mu\nu} e^{i(kz - \omega t)} \right], \tag{1.12}$$

where $C_{\mu\nu}$ is a constant, symmetric "amplitude" metric, $k^\lambda = (\omega/c, k^1, k^2, k^3) = (\omega/c, 0, 0, k)$ is the wave vector pointing in the z-direction, ω is the wave (angular) frequency. The usual dispersion relation $\omega = kc$ is satisfied because the wave vector is null ($k_\lambda k^\lambda = 0$) in the vacuum solution. Under the condition that the perturbation is transverse, we have in general that

$$\partial^\mu h_{\mu\nu}^{\mathrm{TT}} = i C_{\mu\nu} k^\mu e^{ik_\lambda x^\lambda} = 0, \tag{1.13}$$

which implies $k^\mu C_{\mu\nu} = 0$. Like $h_{\mu\nu}^{\mathrm{TT}}$, by definition $C_{\mu\nu}$ must be purely spatial and thus $C_{0\nu} = 0$, and combining both conditions on $C_{\mu\nu}$, we find that $C_{3\nu} = 0$ and the tensor's only nonzero components are where $\mu, \nu \in \{1, 2\}$. The matrix form can be written as

$$C_{\mu\nu} = \begin{pmatrix} 0 & 0 & 0 & 0 \\ 0 & C_{11} & C_{12} & 0 \\ 0 & C_{12} & -C_{11} & 0 \\ 0 & 0 & 0 & 0 \end{pmatrix} \equiv \begin{pmatrix} 0 & 0 & 0 & 0 \\ 0 & h_+ & h_\times & 0 \\ 0 & h_\times & -h_+ & 0 \\ 0 & 0 & 0 & 0 \end{pmatrix}, \tag{1.14}$$

where we have utilized the fact that $C_{\mu\nu}$ must be traceless and symmetric. On the right, we have renamed the coefficients to describe the "plus" ($+$) and "cross" ($\times$) polarization modes of the wave.

We will now derive the scaling relations for a binary system emitting GWs as shown by Eq. 1.3. Consider two masses m_1, m_2 orbiting in a binary far away from the observer at a distance D. Analogously to electromagnetism, we can use a multipole formulation to describe the nature of gravitational radiation. Note that such a formulation treats gravity as a vector (spin-one) field rather than a tensor (spin-two) field; however, it is useful to obtain the approximate scaling relations. The mass monopole, equivalent to the electric monopole, will simply equal $\sum_i m_i$ and does not produce radiation because it is conserved. The mass dipole, equivalent to the electric dipole, will be $\sum_i m_i r_i$ and will also produce no radiation. The first time-derivative will be $\sum_i m_i \dot{r}_i$, which is the constant momentum and therefore cannot produce radiation either. Now we must also consider the equivalent to magnetic dipole radiation. The magnetic moment $\boldsymbol{\mu} \sim \mathbf{r} \times \mathbf{j} \sim \mathbf{r} \times (\rho \mathbf{v})$, where $\mathbf{r}$ is the position vector and $\mathbf{j}$ is the electric current density equal to the charge density ρ times the velocity vector $\mathbf{v}$. Thus, the analogous expression to the magnetic momentum is the angular momentum of the system. Since the second time-derivative of the magnetic moment is what generates magnetic-dipole radiation, we focus on the second time-derivative of the angular momentum, which is zero and therefore no gravitational dipole radiation can be generated.

The next order term is the gravitational quadrupole, again analogous to the electric quadrupole. The power radiated for such a quadrupole is $L \sim \langle \dddot{I}^2 \rangle$, where $I_{jk} \sim \sum_i m_i r_{ij} r_{ik}$ is the second moment of the mass distribution, $\mathcal{I}_{jk}$ is the trace-free part of I_{jk}, and the average occurs over many characteristic periods of the source.

Recall the two masses orbiting each other and assume $m_1 \sim m_2 \sim M$. The amplitude of the gravitational field far from the source (and transverse) will be $h \propto I/D \sim MR^2/D$ (analogous to the electric radiation field $E \sim qa/D$). We require

two time derivatives of the I_{jk} so that in geometrized units (where $G = c = 1$ and mass, length, and time are in equivalent units), the strain is dimensionless. By dimensional analysis, we include the prefactor G/c^4, and

$$h_{jk} \sim \frac{G}{Dc^4} \ddot{I}_{jk}. \tag{1.15}$$

For reference, the full form of the quadrupole formula can be solved with the use of Green's functions and Eq. 1.2, and includes $\ddot{I}_{jk}$ evaluated at the retarded time $t - r/c$ and another factor of 2 out front. We can continue with the approximation and show that Eq. 1.15 can be written as

$$h \sim \frac{G}{Dc^4} \frac{MR^2}{T^2}, \tag{1.16}$$

which yields the result given by Eq. 1.3. See chapter 36 of Misner et al. (1973) and chapter 7 of Carroll (2004) for more information regarding the choices made in our approximations.

BIBLIOGRAPHY

Abbott, B. P., Abbott, R., Abbott, T. D., et al. 2016, Physical Review Letters, 116, 061102

Abbott, B. P., Abbott, R., Abbott, T. D., et al. 2016, Physical Review Letters, 116, 241103

Baade, W., & Zwicky, F. 1934, Proceedings of the National Academy of Science, 20, 259

Backer, D. C., Kulkarni, S. R., Heiles, C., Davis, M. M., & Goss, W. M. 1982, Nature, 300, 615

Carroll, S. M. 2004, Spacetime and geometry / Sean Carroll. San Francisco, CA, USA: Addison Wesley, ISBN 0-8053-8732-3, 2004, XIV + 513 pp.,

Chandrasekhar, S. 1931, ApJ, 74, 81

Comella, J. M., Craft, H. D., Lovelace, R. V. E., & Sutton, J. M. 1969, Nature, 221, 453

Cordes, J. M., Shannon, R. M., & Stinebring, D. R. 2016, ApJ, 817, 16

Detweiler, S. 1979, ApJ, 234, 1100

Dyson, F. W., Eddington, A. S., & Davidson, C. 1920, Philosophical Transactions of the Royal Society of London Series A, 220, 291

Einstein, A. 1915, Sitzungsber. preuss.Akad. Wiss., vol. 47, No.2, pp. 831-839, 1915, 47, 831 Explanation of the Perihelion Motion of Mercury from the General Theory of Relativity

Einstein, A. 1915, Sitzungsberichte der Königlich Preußischen Akademie der Wissenschaften (Berlin), Seite 844-847.

Einstein, A. 1916, Naturwissenschaften, 4, 481

Estabrook, F. B., & Wahlquist, H. D. 1975, General Relativity and Gravitation, 6, 439

Foster, R. S., & Backer, D. C. 1990, ApJ, 361, 300

Gold, T. 1968, Nature, 218, 731

Gold, T. 1969, Nature, 221, 25

Grishchuk, L. P. 2005, Physics Uspekhi, 48, 1235

Hellings, R. W., & Downs, G. S. 1983, ApJL, 265, L39

Hewish, A., Bell, S. J., Pilkington, J. D. H., Scott, P. F., & Collins, R. A. 1968, Nature, 217, 709

Hobbs, G. 2013, Classical and Quantum Gravity, 30, 224007

Hobbs, G., Archibald, A., Arzoumanian, Z., et al. 2010, Classical and Quantum Gravity, 27, 084013

Hofmann, F., Müller, J., & Biskupek, L. 2010, A&A, 522, L5

Hulse, R. A., & Taylor, J. H. 1975, ApJL, 195, L51

Kramer, M., & Champion, D. J. 2013, Classical and Quantum Gravity, 30, 224009

Le Verrier, U. J. 1859, Annales de l'Observatoire de Paris, 5, 1

Manchester, R. N., Hobbs, G. B., Teoh, A., & Hobbs, M. 2005, AJ, 129, 1993

Manchester, R. N., Hobbs, G., Bailes, M., et al. 2013, PASA, 30, e017

Manchester, R. N., & IPTA 2013, Classical and Quantum Gravity, 30, 224010

McLaughlin, M. A. 2013, Classical and Quantum Gravity, 30, 224008

Misner, C. W., Thorne, K. S., & Wheeler, J. A. 1973, San Francisco: W.H. Freeman and Co., 1973,

Olausen, S. A., & Kaspi, V. M. 2014, ApJS, 212, 6

Pacini, F. 1968, Nature, 219, 145

Richards, D. W., & Comella, J. M. 1969, Nature, 222, 551

Romani, R. W. 1989, NATO Advanced Science Institutes (ASI) Series C, 262, 113

Sanidas, S. A., Battye, R. A., & Stappers, B. W. 2013, ApJ, 764, 108

Sazhin, M. V. 1978, SvA, 22, 36

Shao, L., & Wex, N. 2012, Classical and Quantum Gravity, 29, 215018

Shao, L., & Wex, N. 2013, Classical and Quantum Gravity, 30, 165020

Shao, L., Caballero, R. N., Kramer, M., et al. 2013, Classical and Quantum Gravity, 30, 165019

Staelin, D. H., & Reifenstein, E. C., III 1968, Science, 162, 1481

Stairs, I. H., Faulkner, A. J., Lyne, A. G., et al. 2005, ApJ, 632, 1060

Starobinskiĭ, A. A. 1979, Soviet Journal of Experimental and Theoretical Physics Letters, 30, 682

Taylor, J. H., & Weisberg, J. M. 1982, ApJ, 253, 908

Taylor, J. H., & Weisberg, J. M. 1989, ApJ, 345, 434

Weisberg, J. M., Nice, D. J., & Taylor, J. H. 2010, ApJ, 722, 1030

Will, C. M. 1992, ApJL, 393, L59

Will, C. M. 2014, Living Reviews in Relativity, 17, 4

Zhu, W. W., Stairs, I. H., Demorest, P. B., et al. 2015, ApJ, 809, 41